Machine learning-assistant colorimetric sensor arrays for intelligent and rapid diagnosis of urinary tract infection

Jianyu Yang[1†], Ge Li[1†], Shihong Chen[2], Xiaozhi Su[3], Dong Xu[4], Yueming Zhai[5], Yuhang Liu[1], Guangxuan Hu[1], Chunxian Guo[1], Hong Bin Yang[1]*, Luigi G. Occhipinti[6]*, Fang Xin Hu[1]**

[1]School of Materials Science and Engineering, Suzhou University of Science and Technology, Suzhou, 215009, China

[2]School of Chemistry and Chemical Engineering, Southwest University, Chongqing, 400715, China

[3]Shanghai Synchrotron Radiation Facility, Shanghai Advanced Research Institute, Chinese Academy of Sciences, Shanghai, 201204, China

[4]Department of Diagnostic Ultrasound Imaging & Interventional Therapy, Zhejiang Cancer Hospital, Hangzhou Institute of Medicine, Chinese Academy of Sciences, Hangzhou, Zhejiang 310022, China; Wenling Big Data and Artificial Intelligence Institute in Medicine, Taizhou, Zhejiang 317502, China; Key Laboratory of Head & Neck Cancer Translational Research of Zhejiang Province, Hangzhou, Zhejiang 310022, China; Taizhou Key Laboratory of Minimally Invasive Interventional Therapy & Artificial Intelligence, Taizhou Campus of Zhejiang Cancer Hospital, Taizhou, Zhejiang 317502, China

[5]The Institute for Advanced Studies, Wuhan University, Wuhan, Hubei 430072, China

[6]Department of Engineering, University of Cambridge, 9 J J Thomson Avenue, Cambridge CB3 0FA, United Kingdom

†These authors contributed equally

Corresponding authors: cxguo@usts.edu.cn (C. Guo); yanghb@mail.usts.edu.cn (HB. Yang); hufx278@usts.edu.cn (FX. Hu); lgo23@cam.ac.uk (L.G. Occhipinti)

KEYWORDS: colorimetric sensor array, urinary tract infections, Fe single-atom nanozyme, microorganism identification, machine learning

ABSTRACT: Urinary tract infections (UTIs), which can lead to pyelonephritis, urosepsis and even death, are among the most prevalent infectious diseases worldwide, with a notable increase in incidence due to the emergence of drug-resistant pathogens. Current diagnostic strategies for UTIs, such as urine culture and flow cytometry, require time-consuming protocols and expensive equipment. We present here a machine learning-assisted colorimetric sensor array based on recognition ligand-functionalized Fe single-atom nanozymes for the identification of microorganisms at the order, genus, and species levels. Colorimetric sensor arrays are built from the single-atom nanozymes (SANs) Fe_1-NC functionalized with four types of recognition ligands, generating unique microbial identification fingerprints. By integrating the colorimetric sensor arrays with a trained computational classification model, the platform can identify more

than 10 microorganisms in UTI urine samples within one hour. Diagnostic accuracy up to 97% was achieved in 60 UTIs clinical samples, holding great potential for translating into clinical practice applications.

Introduction

Pathogenic microorganisms that can cause a wide range of infectious diseases pose a significant threat to the public health[1]. Urinary tract infections (UTIs) are common diseases caused by the invasion of pathogens in urinary tracts[2]. They can lead to further complications such as pyelonephritis, urosepsis, and even death[3], making them among the most prevalent infection-related diseases worldwide. The main UTI-related pathogens are Gram-negative bacteria (e.g., *Escherichia coli*), Gram-positive bacteria (e.g., Enterococcus faecalis), and fungi (e.g., Candida albicans)[4-6]. The emergence of drug-resistant pathogens has significantly increased the difficulty of treating UTI[7, 8] diseases in recent years. The current standard method for UTIs diagnosis is urine culture, which requires multistep protocols and is time-consuming[9]. Other technologies such as high-throughput sequencing and flow cytometry have also been utilized to detect microorganism in human urines[10, 11]. These diagnostic methods face challenges due to their complex sample preparation processes, equipment cost, and time requirements, hindering their applications.

Recently, other strategies such as colorimetric dipstick, impedimetric method, and microfluidic chip have been reported for pathogens detection in urine samples[12]. Although these methods have the advantages of fast detection, low cost, and high selectivity, they cannot achieve the simultaneous identification and analysis of multiple

microorganisms in urine samples, underscoring the need for innovative diagnostic approaches that can help deliver targeted therapies to reduce the use of antibiotics.

Optical sensing arrays, built with functionalized nanomaterials, have demonstrated great promise as a powerful platform in microbial analysis due to their high sensitivity and rapid response[13-17]. Different optical sensor arrays have been designed for the accurate analysis of microbial strains, bacterial biofilms, and gut microbiota[18-21]. However, the biosensor arrays developed to date primarily rely on mechanisms of electrostatic or hydrophobic interactions, whereby the optical signals utilized for microorganism identification are susceptible to the external environment. Hence, the need to explore sensing materials with unique physicochemical properties and anti-interference ability as a key strategy to achieve accurate microorganism discrimination in clinical urine samples. Single-atom Fe-N-C nanozymes with active sites akin to those of natural enzymes exhibit excellent enzyme-like activities[22]. They catalyze the co-reactive reagent hydrogen peroxide (H_2O_2) into hydroxyl radicals (·OH), superoxide and singlet oxygen, causing 3,3',5,5'-Tetramethylbenzidine (TMB) to transition from colorless to blue, and leading to the generation of an absorbance signal[23-28]. Additionally, modifying their surface with recognition ligands endows these nanozymes with high selectivity towards specific analytes. Consequently, it is anticipated that functionalized Fe-N-C nanozymes could be utilized to develop colorimetric sensing arrays for the accurate diagnosis of UTIs in clinical samples.

With the rapid development of artificial intelligence, the integration of machine learning algorithms has been applied to improve the detection capabilities of these

sensor arrays[29-32]. The use of unsupervised algorithms such as PCA, T-SNE and U-MAP allows to reduce the multidimensional features of complex datasets, and facilitate the following supervised learning steps. Additionally, they can reduce the training time and improve the learning effectiveness[33, 34]. More recently, support vector machine, random forest and other supervised learning methods have been applied to construct the detection model for microbial analysis and disease diagnosis[35, 36]. Thus, the synergistic combination of machine learning algorithms and optical sensing arrays with SANs allows to build an intelligent nanoplatform for rapid and reliable identification of UTI types.

In this study, we present the development of a machine learning-assisted colorimetric nanoplatform (MCN) based on Fe single-atom catalyst (Fe_1-NC) with multiple nanozyme properties for clinical diagnosis of UTIs (Fig. 1a). Four-element colorimetric sensor arrays are built from different types of recognition ligands including boric acid[37], antibiotics[38], D-alanine acid[39] and CTAB[40] that are assembled on the surface of SANs Fe_1-NC, to identify the unique microbial fingerprints (Fig. 1b). Chromogenic mechanism of microbial inhibition of Fe_1-NC nanozymes is explored. Notably, both the Fe and N active sites exhibit a crucial role in the microorganism identification. Coupling with U-MAP algorithms (Fig. 1c), the main UTI-related microorganisms with varied order, genus and species levels can be accurately identified. Furthermore, an SVM algorithm was developed as a mathematical model for the classification of healthy people, bacterial, and fungal infectious disease urine samples (Fig. 1d), showcasing a diagnostic accuracy up to 97% on 60 clinical samples.

This approach represents a significant advancement in UTI diagnostics, offering a promising solution for the rapid, accurate, and cost-effective identification of UTIs in clinical settings.

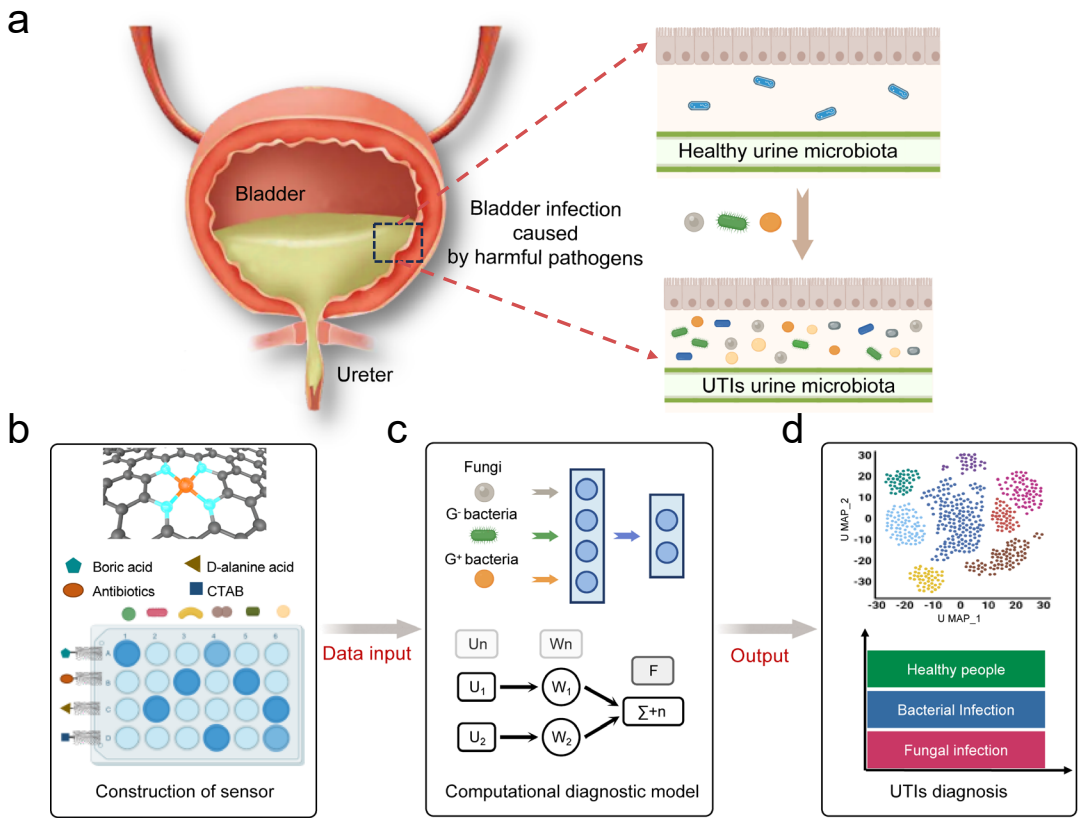


Figure 1. Schematic diagram of the intelligent diagnostic nanoplatform based on Fe_1-NC nanozymes for rapid and accurate diagnosis of UTIs. (a) The situation of microbiota in UTIs patients. UTIs are common diseases caused by the direct invasion of harmful pathogens in bladder. (b) Construction of colorimetric sensing system for microorganism identification based on the four-recognition molecular functionalized Fe_1-NC nanozymes. (c) The machine learning assisted computational diagnostic model for microbiological assay for UTI diagnosis. (d) Performance of the detection model for UTI diagnosis.

Experimental Section/Methods

***Preparation of Fe_1-NC and NC nanozymes*:** Fe_1-NC catalyst was prepared with the strategy reported in our previous work[41]. 9 g of melamine, 1.6 g of L-alanine and 0.06 g of iron (II) acetate were mixed and ball-milled for 5 h to blend them into a homogeneous precursor. Then, the obtained precursor was calcinated at high temperature in two stages. In the first stage, the precursor was pyrolyzed in a tube furnace from 30 ºC to 600 ºC at a rate of 3 ºC min^{-1} and held at 600 ºC for 2 h. Then, carbonized from 600 ºC to 900 ºC at a rate of 2 ºC min^{-1} and held at 900 ºC under an argon atmosphere for 1 h. In the second stage, after cooling down to room temperature, the sample was soaked in 1 M HSO_4 acid at 80 °C for 24 h. After that, the acid-washed sample was heated again at 850 °C undern argon atmosphere for 1 h. Nitrogen-doped carbon (NC) catalyst was synthesized by the same procedure without adding iron (II) acetate. The specific fabrication steps for four types of recognition ligands functionalized on Fe_1-NC nanozymes are described in the Supporting Information.

***Microorganism identification*:** Specific culture method of microorganism is provided in the Supporting Information. The microorganism solution was centrifuged 3 times (6000 rpm for 5 min) by PBS (0.01 M, pH=7.4), while diluted to the required concentration for the assay. Then, 25 μL four types of catalysts (20 μg/mL), 25 μL bacteria suspension, 25 μL TMB (5 mM) and 25uL H_2O_2 (0.1 M) were added into 150 uL PBS (0.01 M, pH=6.0). After incubating for 30 min at 37°C, the UV-vis absorbance (λ=652 nm) of the solution was measured by UV spectrophotometer or microplate reader, in which A_0 and A represented the colorimetric signal of catalysts in the absence

or presence of bacteria, respectively. Each sample was replicated for six times. The obtained data were normalized by $(A-A_0)/A_0$. Finally, PCA, T-SNE, U-MAP and K-means were used to process the final dataset with SPSS Modeler 18.0 and Python (3.10.4) software.

***Clinical UTIs diagnosis*:** To construct the mathematical diagnosis model, microarray data of patients diagnosed with UTIs were obtained from Zhejiang Cancer Hospital (Taizhou District). The UTIs urine samples were first selected and labeled as bacterial or fungal infections (40 samples in each category). The diluted urine samples (urine: water, 1:10) were added to the sensing system and incubated in 96-well plates at 37°C. Following the above experimental steps, the UV-vis absorbance (λ=652 nm) was monitored by BioTek microplate reader. Then, the obtained dataset was processed using the U-MAP method, reducing the four-dimensional data into two-dimensional. Then, we trained a linear SVM algorithm based on this dataset to distinguish between bacterial and fungal infections. Finally, 60 UTI samples were selected for the experimental phase implementation, to determine the detection performance of the diagnostic model.

Results and Discussion

Morphological and structural characterizations

Fe_1-NC catalyst was prepared using the similar synthesis method of A-Ni-NC single-atom catalysts reported in our previous work[41]. The morphology of Fe_1-NC catalyst was characterized by scanning electron microscope (SEM) and transmission electron microscope (TEM), revealing its two-dimensional sheet structure as shown in

Figures S1a and S1b. Atomic force microscope (AFM) measurements confirm a similar morphology of Fe_1-NC with graphene (Fig. 2a) with a thickness of approximately 2.8 nm. Energy dispersive X-ray (EDX) spectrometer showed that C, N and Fe atoms are uniformly distributed throughout the carbon substrate (Fig. 2b). X-ray diffraction (XRD) spectrums of Fe_1-NC and N-doped carbon (NC) catalyst are reported in Fig. 2c, with evidence of only two broad diffraction peaks of amorphous carbon (002) and (004) at 26.2° and 44.0°, respectively. Besides, no diffraction peaks of metallic Fe were observed for Fe_1-NC, indicating that neither Fe-derived particles nor crystalline Fe compounds exist in Fe_1-NC [42]. In addition, high density bright spots in the aberration-corrected high-angel annular dark-field scanning transmission electron microscopy (HAADF-STEM) image of Fe_1-NC further confirms that Fe species are atomically dispersed on the carbon substrate (Fig. 2d). The content of Fe in Fe_1-NC is around 2.2 %, quantified by inductive coupled plasma (ICP) emission spectrometer.

Chemical composition and elemental states of Fe_1-NC were investigated by XPS (Fig. S2). The binding energies of Fe $2p_{3/2}$ and Fe $2p_{1/2}$ in Fe_1-NC were 709.6 and 722.5 eV, indicating that the valence of iron species in Fe_1-NC are close to +2 as shown in Fig. 2e. The high-resolution N 1s spectra of NC (Fig. 2f) could be deconvoluted into four main species, pyridine N (397.8 eV), pyrrole N (399.8 eV), quaternary N (400.8 eV) and oxidized N (403.1 eV)[43]. Compared with NC, N 1s spectra of Fe_1-NC showed an additional Fe-N at 398.7 eV, indicating Fe atom coordinated with N atom. X-ray absorption spectroscopy (XAS) was further performed to investigate the oxidation number and coordination information of Fe center in Fe_1-NC. As shown in Fig. 2g, for

Fe_1-NC, the absorption edge energy of Fe K edge adsorption is ~ 7180 eV, which is close to that of FePc, confirming the +2 valence of Fe in Fe_1-NC. The Fourier-transformed (FT)-EXAFS spectra (Fig. 2h) exhibit a primary peak at around 1.47 Å for both Fe_1-NC and FePc, which is owing to Fe-N scattering[44]. Fe-Fe bond at around 2.2 Å does not appear for Fe_1-NC compared with Fe foil, confirming atomic dispersion Fe atoms in Fe_1-NC. The quantitative structural parameters of Fe in Fe_1-NC are obtained by the fitting EXAFS curve (Fig. 2i and table S1). Results show the coordination numbers of the single Fe atom are 4.68 and 4.20 for FePc and Fe_1-NC, respectively, with bond distances of 1.82 and 1.98 Å, respectively, indicating Fe atom coordinated with four N atoms. Supplementary Fig. S3 shows the k3-weighted k-space spectra of different materials.

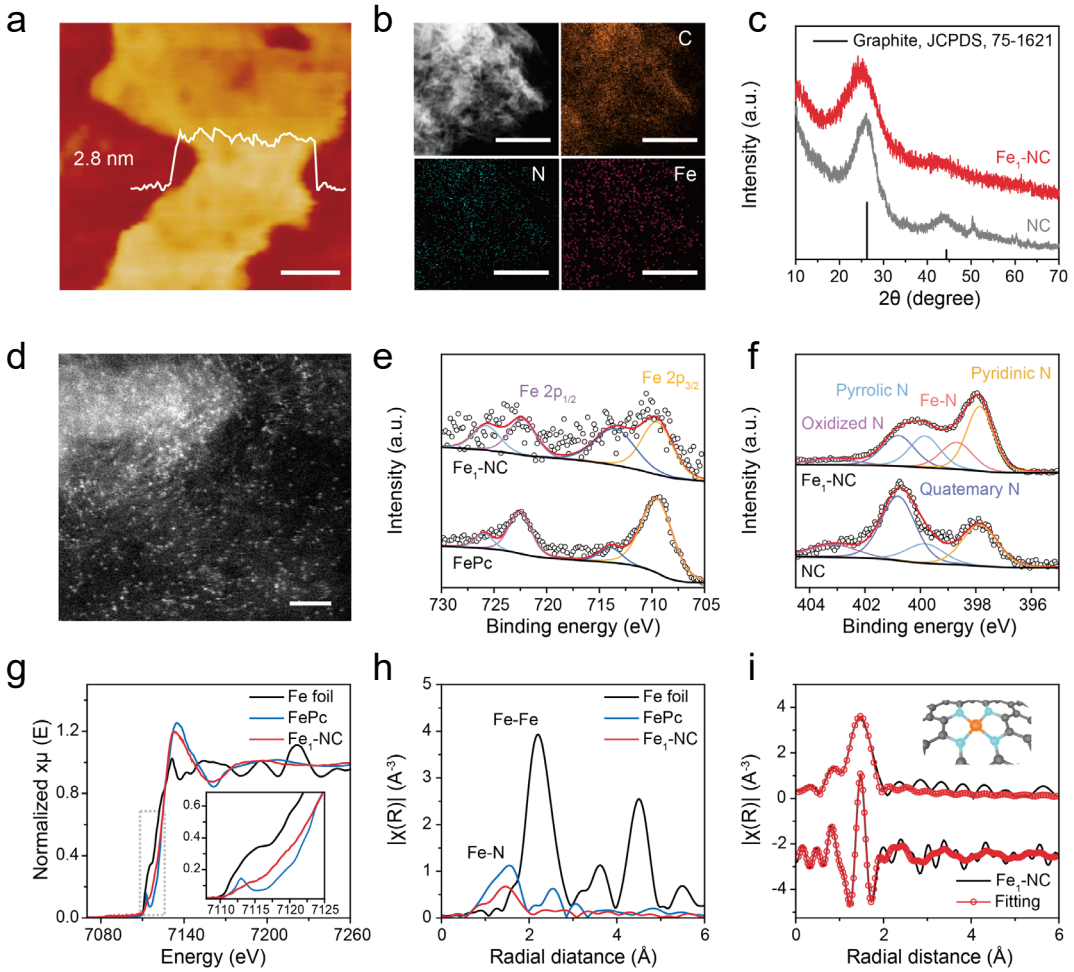


Figure 2. The morphological and structural characterization of Fe$_1$-NC. (a) AFM image of Fe$_1$-NC. (b) EDX elemental mapping of Fe$_1$-NC. Scale bars in B are 500 nm. (c) XRD pattern of Fe$_1$-NC and NC. (d) AC-HAADF-STEM image of Fe$_1$-NC, scale bar in D is 2 nm. (e) Fe 2p high-resolution spectrum of Fe$_1$-NC and FePc. (f) N 1s high-resolution spectrum of Fe$_1$-NC and NC. (g) K-edge XANES spectra of Fe$_1$-NC, FePc, and Fe foil. (h) Fourier-transformed (phase uncorrected) Fe K-edge EXAFS spectra. (i) First-shell fitting of the Fourier transformation of the EXAFS spectrum of Fe$_1$-NC (the EXAFS spectrum was fitted using the FEFF 8.2 code). Inset: the structure diagram of Fe$_1$-NC.

Multiple enzyme-like activities of Fe_1-NC nanozymes

Bladder infection is the most common type among UTIs that occur when pathogens enter the urethra, and infect the urinary tract (Fig. 1a). The identification of microorganism in human urine samples is critical for UTIs diagnosis. Surface chemical structural differences of microorganisms such as Gram-positive (G^+) bacteria, Gram-negative (G^-) bacteria and fungi provided theoretical guidance for the functionalization of Fe_1-NC sensor[45, 46], as shown in Fig. 3a. Specific chemical complex on microbial surface such as saccharide, protein, peptide, and other membrane structures can be identified as recognition molecules for microbial discrimination. Multiple enzyme-like activities of Fe_1-NC and NC were evaluated by colorimetric method with a chromogenic substrate 3,3',5,5'-tetramethylbenzidine (TMB) as shown in Fig. 3b. The UV-vis absorption spectrum of colorless TMB showed no absorption peak in the wavelength range of 400~800 nm. After addition of H_2O_2 (10 mM), NC (2 μg mL^{-1}) and Fe_1-NC (2 μg mL^{-1}) into TMB solution (0.5 mM), separately, absorbance peaks at 652 nm were observed with color of solutions turning blue. Results indicated that both Fe and N sites could act as catalytic active centers for reactive oxygen species (ROS) generation, which can induce TMB oxidation. Among which, absorption peak of Fe_1-NC mixed with TMB was the highest, indicating the strongest enhancement of catalysis of TMB oxidation by Fe active site. To investigate the TMB oxidation process, NC and Fe_1-NC were mixed with H_2O_2 as co-reactive reagent, both of which showed a darker blue color and enhanced absorbance than

that without H_2O_2. Results suggested that the incorporation of H_2O_2 could significantly increase the effectiveness of the oxidation of TMB. Moreover, Fe_1-NC behaved a much higher catalytic performance than NC, owing to the intrinsic activity of SANs. Moreover, during the reaction between Fe_1-NC and TMB-H_2O_2, O_2 bubbles were clearly observed, which proved that Fe_1-NC has catalase (CAT) catalytic activity.

To fully study the mechanism concerning Fe_1-NC facilitate TMB chromogenic, ROS generated in the catalytic system was investigated by Electron Spin Resonance (ESR) spectroscopy. As displayed in Fig. 3c and 3d, 5, 5-Dietyl-1-Pyrroline -N-oxide (DMPO) and 2, 2, 6, 6-tetramethylpiperidine-1-oxyl (TEMPO) were utilized as free radical trap for superoxide radicals ($O_2^{\cdot-}$) and singlet oxygen ($^1O_2$). For NC and Fe_1-NC, both $O_2^{\cdot-}$ and $^1O_2$ signals were captured, which were much stronger than that for H_2O_2, indicating the oxidase (OXD)-like and superoxide dismutase (SOD)-like properties. Results shown NC behaved stronger OXD-like properties, while Fe_1-NC demonstrated better SOD-like properties. The signal intensities were significantly strengthened with addition of H_2O_2, which attributed that NC and Fe_1-NC could catalyze H_2O_2 generating oxygen to promote the production of more $O_2^{\cdot-}$ and $^1O_2$, showing catalase (CAT)-like property. Besides, Fe single-atom doped of catalyst could convert H_2O_2 into more $^1O_2$ through the Russell mechanism. The peroxidase (POD)-like activity was also investigated as shown in Fig. 3e, there were no typical hydroxyl radicals (·OH) signals for neither pure H_2O_2 (gray curve), NC

(pale yellow curve), Fe_1-NC (bluish violet curve) nor mixture of NC and H_2O_2 (dark green curve), indicating non or weak catalytic activity. As for the mixture of Fe-NC and H_2O_2, complex peaks were detected (Fig. 3e, purple curve). This might owe to the influence of dissolved O_2, which was catalyzed by Fe_1-NC to produce other radicals. Under N_2 atmosphere, as shown in turmeric curve of Fig. 3e, four resonance peaks were detected with resonance intensities of 1 : 2 : 2 : 1, indicating the production of ·OH attribute to the POD-like activity of Fe_1-NC. Results illustrated that NC possessed OXD-like, SOD-like, and CAT-like activity. The introduction of Fe active site could further enhance the catalytic performance of Fe_1-NC, and it also demonstrated POD-like activity, showing dual active site of Fe and N in Fe_1-NC (Fig. 3f). Hence, the multi-enzyme properties of Fe_1-NC can significantly boost the sensitivity of the constructed colorimetric sensor based on TMB system, which could show merit in microorganism infections diagnosis.

Specific complex chemicals on microbial surface such as saccharide, protein, peptide, and other membrane structures can be identified as recognition molecules for pathogen discrimination. Nanomaterials with diverse recognition ligands can be used for microbial identification at the microorganism-material interface. To recognize target microorganisms, four ligands including aminobenzeneboronic acid (BA), vancomycin (Van), D-alanine (D-ala) and cetyltrimethylammonium bromide (CTAB) were selected to construct the array sensing unit.BA was selected as the ligand to realize the classification of

microorganisms due to the difference of saccharides on the surface of microorganisms. Van can bind with D-ala in the cell wall of G^+ bacteria and inhibit the synthesis of peptidoglycan. Hence, selecting Van as the ligand can achieve G^+ bacteria identification. Based on the differences of amino acids required for cell wall synthesis between bacteria and fungi, D-ala was selected as the ligands to achieve accurate classification. There are numerous phosphate groups in the cell wall of microorganisms, and their surface presents negative charges under physiological conditions. The ammonium salt CTAB ligand can display the difference of surface charge of microorganisms. Diverse recognition ligands can reflect the chemical difference of microbial surface microenvironment from multiple dimensions, providing a theoretical basis for the recognition of microorganisms. In this work, the EDC/NHS cross-linking method was utilized to modify the surface of Fe_1-NC catalyst with these four recognition ligands.

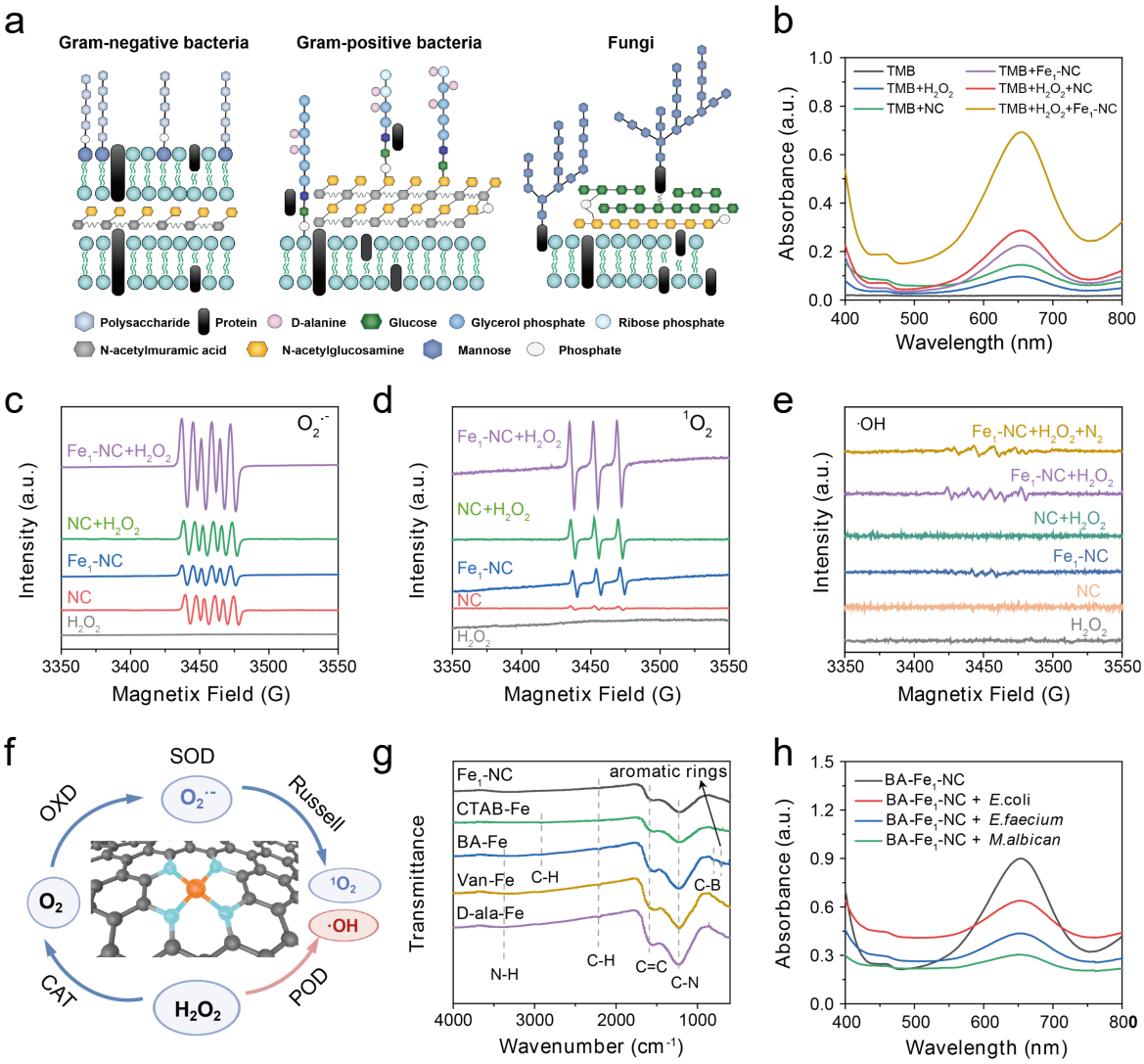


Figure 3. Characterization of multi-enzyme activities of Fe$_1$-NC. (a) The surface chemistry of three types of microorganisms including G$^-$ bacteria, G$^+$ bacteria and fungi. (b) UV-vis absorption spectrum of catalytic systems based on Fe$_1$-NC and NC in phosphate buffer solution (PBS, pH 6.0, 10 mM). ESR spectrum: (c) TEMPO-$O_2^{\cdot -}$ (d) DMPO-$^1O_2$ (e) DMPO-·OH. (f) Schematic of multiple enzyme-like activities of Fe$_1$-NC nanozyme for catalyzing H_2O_2. (g) FTIR spectrum of Fe$_1$-NC and four recognition ligand functionalized Fe$_1$-NC; (h) UV-vis absorption spectrum of BA-Fe$_1$-

NC upon addition of three types of microorganism (OD_{600} = 0.01) in PBS (pH 6.0, 10 mM).

FT-IR analysis was performed to investigate whether the four ligands have been successfully modified on Fe_1-NC catalyst. As shown in Fig. 3g, peaks at 709 cm^{-1} and 800 cm^{-1} were originated from the bending vibration of the benzene ring on the phenylboronic acid and the stretching vibration of C-B, respectively. The peak at 2927 cm^{-1} was derived from the C-H stretching vibration on alkanes in CTAB and BA. The stretching vibration band of -NH- at 3370 cm^{-1} is the characteristic of Van and D-ala ligand. Furthermore, the surface ligands on Fe_1-NC were investigated by XPS spectroscopy (Fig. S4). The specific Cl 2p peak of Van-Fe_1-NC and B 1s peak of BA-Fe_1-NC were displayed in Fig. S5a and Fig. S5b, respectively, which fully indicated that BA as well as Van were successfully modified in Fe_1-NC. As shown in Table S2, the content of N and O elements in Fe_1-NC were significantly increased with the modification of CTAB and D-ala, confirming that these two ligands were modified on Fe_1-NC. The above results suggested that these four diverse ligands functionalized Fe_1-NC were successfully prepared.

SEM analysis were conducted to explore the specific binding between Fe_1-NC and the above three microorganism. We selected BA-Fe_1-NC as the representative sensing units. All the microbial cells aggregated together with BA-Fe_1-NC as bridges, and some of them were even buried with BA-Fe_1-NC "coatings" (Fig. S6). This phenomenon proved that the prepared functionalized Fe_1-NC has excellent binding ability toward

target microorganism. The catalytic activity of the ligand-functionalized catalysts was also investigated, which did not change significantly compared with Fe_1-NC (Fig. S7). Subsequently, *E. coli O157:H7* (G^-), *E. faecalis* (G^+), and *C. albicans* (fungi) were selected as representatives to examine the changes in the catalytic performance of functionalized Fe_1-NC after incubation with microorganism. Firstly, the unmodified Fe_1-NC was determined after incubation of microorganism. It is worth noting that the absorbance of Fe_1-NC catalyst did not change significantly upon addition of microorganism (Fig. S8a). However, the absorbance value of the BA-functionalized Fe_1-NC catalyst significantly decreased following the addition of the target microorganism, as illustrated in Fig. 3h. The introduction of three types of microorganisms – *E. coli O157:H7* (G^-), *E. faecalis* (G^+), and *C. albicans* (fungi) – resulted in a varied rduction in absorbance, attributable to the specific biomolecules present on their surfaces. Results showed that Van, CTAB and D-ala functionalized Fe_1-NC induced similar trends with BA-Fe_1-NC upon incubation with different microorganisms (Fig. S8b-d). To further explore the N active site on the sensing system, the catalytic performance of the four ligands functionalized NC was investigated (Fig. S9), which reported a similar phenomenon of Fe_1-NC but weaker effect. Notably, both the Fe and N active sites displayed a crucial role in the microorganism discrimination. These observations provided the foundation for the following UTI diagnosis.

Construction of taxonomic models for microbial identification

More than 10 microorganisms were selected as the target analyte, including G^- bacteria and G^+ bacteria and fungi, which accounted for more than 90% of the microorganisms in human urine with UTIs (Table S3). To improve the discrimination ability of the sensing array, the experimental conditions for sensing including pH effect of PBS, reaction time, and concentration of Fe_1-NC were carefully investigated. *E. coli O157:H7 and* BA-Fe_1-NC was chosen as the representatives, respectively. By mixing a series of PBS with different pH values with *E. coli*, the optimal colorimetric signal was obtained at pH 6.0 (Fig. S10a). The reactions of Fe_1-NC to *E. coli* took around 30 min to reach equilibria (Fig. S10b). In addition, the colorimetric response of Fe_1-NC toward *E. coli* reached the most sensitive response with a concentration of 20 ug/mL (Fig. S10c). In subsequent experiments, these optimized conditions were employed for the analysis of microorganisms. Colorimetric sensor based on Fe_1-NC catalyst was applied to evaluate the common microorganisms in human urine. As expected, the functionalized Fe_1-NC displayed various binding ability to target microorganism and generated the unique colorimetric signal fingerprints for microbial classification (Fig. S11). The specific colorimetric response of these four functionalized Fe_1-NC towards G^- bacteria, G^+ bacteria and fungi were shown in Fig. 4a. BA-Fe_1-NC and CTAB-Fe_1-NC displayed the sensitive response to fungi, while Van-Fe_1-NC and D-ala-Fe_1-NC were willing to bind with G^+ bacteria. This phenomenon was attributed to the chemical structure of microorganisms and the surface ligand properties of Fe_1-NC.

There might be different concentrations and various types of microbial samples in clinical diagnosis of urinary tract infectious diseases, which were investigated in detail to study the discriminative capability of the sensing system. *E. coli O157: H7* at a wide concentration range from OD_{600} = 0.00001 to 0.1 can be well classified, both in PBS (Fig. 4b) and human urine (Fig. 4c). The samples with microbial concentration in urine higher than 10^5 cfu/mL (OD_{600}= 0.0001) are diagnosed as UTIs. The system could realize the microbial detection as low as 10^4 cfu/mL (OD_{600}= 0.00001), which showed the potential application in actual samples. Then, the mixtures of *E. coli* and *S. aureus* were selected as the analyte to investigate the classification performance of the proposed sensor for coexisting microorganism. The U-MAP plots displayed that the mixtures of analyte were completely separated, five blended microorganism samples could be reasonably clustered and assigned to respective groups (Fig. 4d). For the mixtures of various types of *E.coli* strains, the sensor could achieve accurate identification and group them appropriately in the order of molar ratios (Fig. 4e). We also investigated the recognition of the sensing system for the mixtures of *E. coli* and *S. aureus*, *and* the mixtures of various types of *E.coli* strains in human urine environments. The sensor array has successfully realized the discrimination of the microbial mixtures even in human urine samples (Fig. S12). Considering that the surface chemical structure of the microorganism might be affected by the local growth environment, numerous samples should be measured to increase the accuracy of microbial fingerprint data. Then, we investigated glucose (50 mM), Na^+ (150 mM), K^+ (90 mM), Ca^{2+} (3 mM), urea (4mM), human serum albumin (10mg/ml),

ascorbic acid (50 μM), uric acid (150 μM) and other common interfering substances on the colorimetric sensing system (Fig. 4f). The effect of common thiolate compounds on the sensing system was also evaluated. Cysteine (50 μM) and glutathione (5 μM) have negligible effects on the colorimetric signal of the system (Fig. S13). As shown in Fig. 4g, the impact of these substances on the system could be negligible, indicating good selectivity. In addition, the features of four functionalized Fe_1-NC by the same microorganism showed no significant difference after stored for different days, indicating the stability of nanoplatform (Fig. S14). Results indicated four types of functionalized Fe_1-NC could be utilized as the colorimetric sensing array for UTIs diagnosis.

Subsequently, a taxonomic model was constructed owing to the multiple enzyme properties of Fe_1-NC for target microorganism discrimination. Firstly, three types of unsupervised dimension-reducing algorithms, including PCA, T-SNE and U-MAP were selected to evaluate the discrimination of microorganism by the colorimetric sensing system. The colorimetric signals were measured 6 times for each analyte, producing 4 channels × 10 analytes × 6 replicates data set for the microbial taxonomic classification. The four-dimensional optical signals were reduced into a 2D plot by dimensionality reduction with the above algorithms. The first two canonical factors after dimensionality reduction were visualized as a 2D plot, which accurately exhibits numerous isolated clusters. Then we chose the K-means algorithm, a clustering algorithm that classifies analytes based on the Euclidean distance of the target to the central point, to investigate the classification of microbial strains by three algorithms

(Fig. S15a-c). For microbial classification at species level, T-SNE and U-MAP algorithms showed significant effects in the differentiation of 10 microorganisms, with the accuracy of 100% (Fig. S15e, f). However, the accuracy of PCA algorithm was 91.7%, and some strains of *E. faecalis* were misdiagnosed as *K. pneumoniae* (Fig. S15d). We further investigate the classification effect of these dimension-reducing methods on microorganism at the kingdom level. The classification accuracy of K-means algorithm for PCA (Fig. S15g), T-SNE (Fig. S15h) and U-MAP (Fig. S15i) data set was 75%, 65%, and 100% respectively. Given the excellent performance of U-MAP in microbial classification, it was selected as a dimensionality reduction algorithm for subsequent studies.

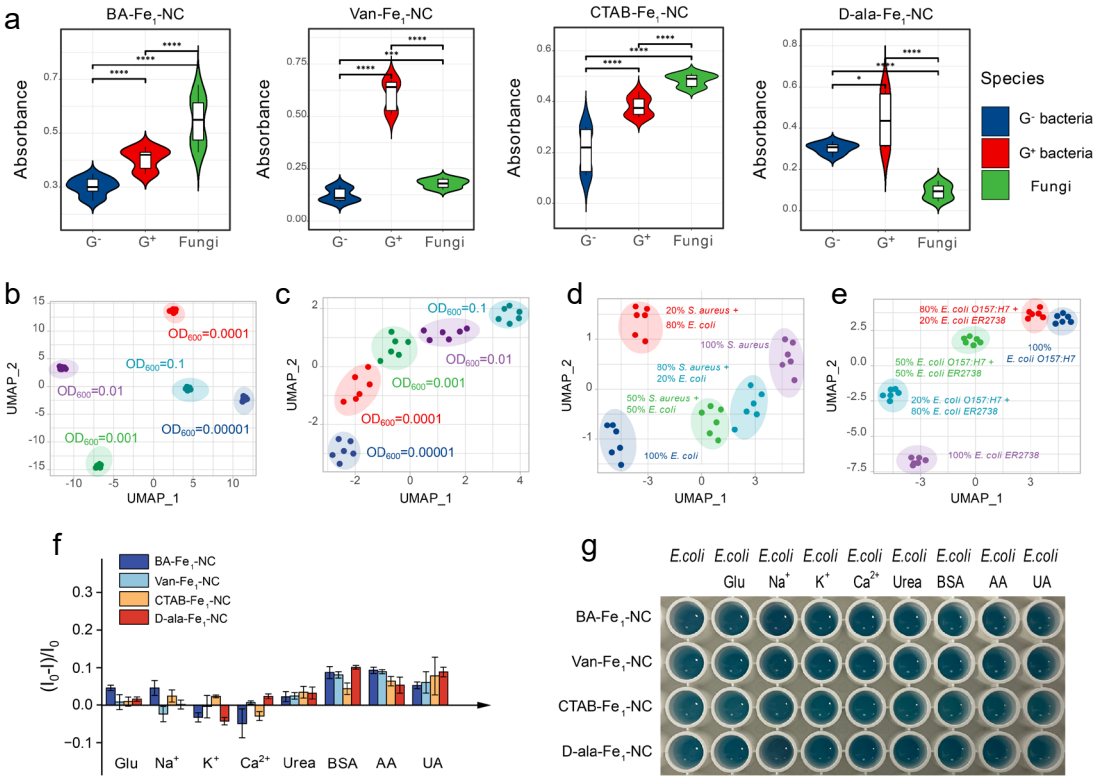


Figure 4. The interactions between functionalized Fe1-NC and microorganisms. (a) The average colorimetric response of BA-Fe1-NC, Van-Fe1-NC, CTAB-Fe1-NC

and D-ala-Fe_1-NC towards G^- bacteria (blue), G^+ bacteria (red) and fungi (green). The concentration of the microorganism was set at OD_{600} = 0.01. Canonical score plots for the sensor array based on functionalized Fe_1-NC towards different concentrations of *E. coli O15:H7* (OD_{600}=0.00001, 0.0001, 0.001, 0.01, 0.01) in PBS (b) and artificial human urine (c) by U-MAP. Canonical score plot against *S. aureus* and *E. coli* mixtures (d), *E. coli O15:H7* and *E. coli ER2738* mixtures (e) by U-MAP. The total concentration of the mixture was set at OD_{600}=0.01. (f) The common interfering substances including Glucose, Na^+, K^+, Ca^{2+}, urea, human serum albumin, ascorbic acid, uric acid on the colorimetric signal in the presence of *E. coli O157:H7*. (g) The color rendering images of the corresponding the solutions. All these samples are prepared in PBS (pH 6.0, 10 mM), the absorbance of the sensing system was collected at 652 nm.

Different taxonomic levels including kingdom, species, and strains were further investigated, separately, to achieve the microbial classification (Fig. 5a). Firstly, Gram-negative positive bacteria, Gram-positive bacteria, and fungi were selected as the analytes to study the identification performance of the system at the kingdom level strains. Subsequently, according to the reported clinical diagnosis of microorganisms in urine of patients with UTIs, the species level strains were chosen as four G^- bacteria (*E. coli*, *K. aerogenes*, *P. aeruginosa*, and *P. vulgaris*), four G^+ bacteria (*E. faecalis*, *E. faecium*, *S. aureus*, and *S. epidermidis*) and two fungi (*C. albicans* and *C. glabrata*). As we all know, microbial drug susceptibility is constantly evolving, and even microbial strains of the same species display significantly different susceptibilities to antibiotics.

In the process of bacterial infection, pathogens with antibiotic resistance tend to cause more therapeutic difficulty. *E. coli* is the most frequent microorganism associated with UTIs. Therefore, in this study, we examined different subtypes of three drug-resistant *E. coli* and two non-resistant *E. coli* to investigate the classification at the strain level. Results showed the proposed sensor array behaved significant performances in kingdom (Fig. 5b), species (Fig. 5c), and strains (Fig. 5d) level classification. These results suggest that our developed sensor array has the potential for application in the analysis of microorganisms in clinical diagnostics. Moreover, the separate clusters of microorganisms (Fig. 5e-g) indicated that these four colorimetric signal features of sensor array enabled microorganism identification at three levels without any overlap, with all the accuracies of 100% (Fig. 5h-j). These results demonstrated that U-MAP algorithm enabled the colorimetric strategy to pinpoint the microbial identification.

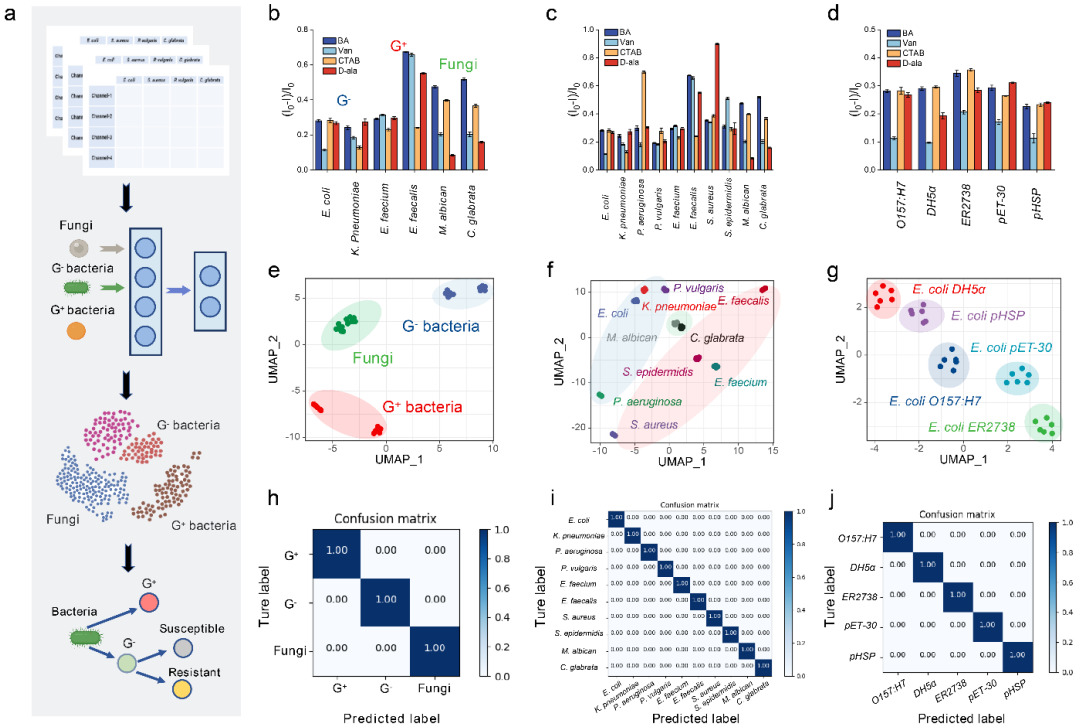


Figure 5. Identification of microorganisms at different taxonomic levels. (a) Construction of the U-MAP model for microorganism identification. The colorimetric fingerprint for microorganism identification at the kingdom level (b), species level (c) and strain level (d) by U-MAP. 2D dimensionality reduction plot for microorganism identification at the kingdom level (e), species level (f) and strain level (g) by U-MAP. The confusion matrix for microorganism identification at the kingdom level (h), species level (i) and strain level (j) by U-MAP. All these samples are prepared from human urine. The concentration of the microorganism was set at OD_{600} = 0.01.

Diagnosis of urinary tract infection disease

Urinary tract is a common site of microbial infection in adults. UTIs are commonly caused by bacteria and fungi pathogens (Fig. 6a). Due to its advantages in dealing with binary classification problems and the number of samples in this experiment, we have utilized the Support Vector Machine (SVM) as the supervised learning algorithm to build the effective model classifier for UTIs diagnosis[47]. A training cohort containing numerous UTIs urine samples (healthy people, bacterial infection, and fungal infection) was first used to train the algorithm by SVM. The obtained classifier can perform arithmetic operations, such as weighting, summation and subtraction, to respond to colorimetric signals in the system and report results in the form of bacterial or fungal infection. The detailed computing process for UTIs diagnosis was demonstrated (Fig. 6b). First, two-dimensional data, U_1 and U_2 undergo weighted multiplication after U-MAP dimension reduction. The multiplication is calculated as [W*n* × U*n* = A*n*]. Here, W*n* represents the weight predetermined by the model, and A*n* represents the weighted

multiplication. Significantly, the weights were limited to integers less than 10 and performed the corresponding mathematical operations, which is beneficial for the subsequent output computation. Then, the two-dimensional data A_1 and A_2 inputs are summed for comparison ($F=A_1 + A_2 + n$). At last, the classification result is reported according to the F values. The critical value of the system is set to 0. If the diagnostic result is lower than 0, it is healthy sample, if it is higher, it is UTIs sample. For the identification of infection type, the U_1 and U_2 data are input into a new function and perform the same calculation process as above. If the classifier output is lower than 0, it is bacterial infection, if it is higher, it is fungal infection.

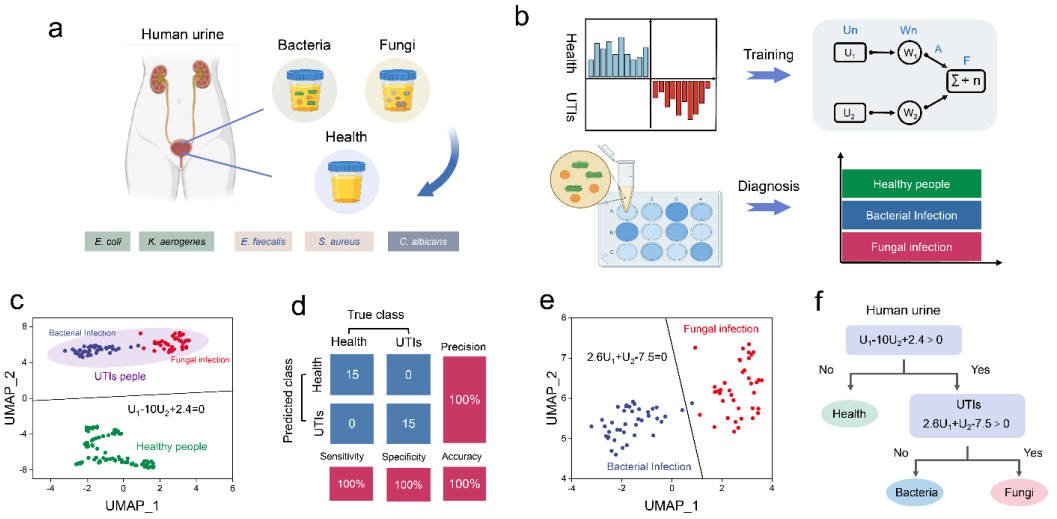


Figure 6. Validation of the colorimetric sensor based on functionalized Fe_1-NC. (a) Two common types of microbial infection in UTIs. (b) Schematic diagram of the machine learning-assistant diagnosis model for UTIs diagnosis. (c) Performance of the detection model with data from the training set (80 healthy samples and 80 UTIs samples). (d) Performance of the detection model with data from the training set (40 bacterial infection and 40 fungal infection). (e) A classification model for the diagnosis

of UTIs infection type. (f) Classification results of the Fe_1-NC based system with 45 clinical samples for the diagnosis of infection type.

To demonstrate that our method can be a reliable nanoplatform for the UTIs diagnosis, we chose human urine with adding microorganism for further experiments. For the bacterial and fungal infections diagnosis, the total accuracy in artificial urine was100% (fig. S16). Similarly, the satisfactory results were also obtained in the diagnosis of G^- and G^+ bacterial infections (fig. S17), and the accuracy was 95%. Then, we collected the clinical samples to further prove that the proposed detection model behaves high accuracy for UTIs diagnosis. The data set contained 160 real human urine samples (80 health, 80 UTIs including 40 bacterial infection and 40 fungal infection) was first used to train the detection model by U-MAP and SVM. Then, the mathematical detection model (U_1-$10U_2$+2.4=0) was employed to evaluate the diagnosis performance of unknown clinical samples (Fig. 6c). All the testing data (15 healthy samples and 15 UTIs samples) were identified correctly with a sensitivity of 100%, a specificity of 100%, and a precision of 100% (Fig. 6d). The total accuracy of this method in human urine samples was 100% (Fig S18a). To further determine the type of infection, the UTIs data set (40 bacterial infection and 40 fungal infection) was utilized to train a new mathematical model (Fig 6e). The specific diagnosis process is displayed in Fig 6f. The U_1 and U_2 undergo the new calculations (U_1-U_2+2.4) to identify the type of infection. As shown in fig. S18b, only 2 bacterial infection sample was misdiagnosed as fungal infection, and the remaining 13 bacterial infection samples and 15 fungal infection samples were classified correctly with the total accuracy of 93%.

(Fig. S18c). Compared with the existing methods (Table S4) for UTIs diagnosis, the constructed nanoplatform showed some advantages such as high accuracy and fast detection speed. The extensive collection of training data, combined with the rational employed of machine learning algorithms, can perform UTIs intelligent diagnosis. The gold standard for human urine microorganism analysis in clinics is urine culture. It usually takes several days to determine the type of UTIs, as its complex programs require more human and financial resources to culture and analyze bacteria. In addition, flow cytometry can be utilized to achieve UTIs diagnosis, but the equipment is expensive and data turnaround time is slow. Dry urinalysis is a convenient and cost-effective method for detecting UTIs at home. However, its accuracy needs to be improved. The proposed diagnostic strategy, combining functionalized Fe_1-NC with machine learning algorithms to build a detection model, significantly improves UTI diagnoses accuracy. These results verified that the SVM-based classifier model could perform computation as designed for UTIs diagnosis in clinical applications.

Conclusion

The intelligent diagnosis of clinical UTIs is achieved through the construction of a machine learning-assisted MCN based on Fe_1-NC functionalized with recognition ligands. The Fe and N species in Fe_1-NC act synergistically as active sites, facilitating multiple oxidase (OXD), superoxide dismutase (SOD), catalase (CAT) and peroxidase (POD)-like activities. Colorimetric sensor arrays, built from the Fe_1-NC functionalized with four types of recognition ligands, enable the generation of microbial identification fingerprints. With the assistance of machine learning algorithms, a training model for

the diagnosis of UTIs has been developed. Furthermore, the SVM algorithm has been utilized to construct a mathematical detection model for diagnosing bacterial and fungal infections. Integrating colorimetric sensor arrays with U-MAP algorithms allowed the identification of microorganisms in UTI-affected urine samples across various orders, genera and species levels. Notably, more than 10 microorganisms in UTI urine samples can be analyzed within one hour, enabling rapid screening and achieving an intelligent diagnosis with an accuracy of up to 97% in 60 clinical samples. The method presented in this study, demonstrating rapid response and convenient operation, offers significant advantages over current UTI diagnostic strategies, such as urine culture and flow cytometry, and holds great potential for practical clinical application in UTI diagnosis. The machine learning-assisted colorimetric sensor arrays presented here could be further extended to design other intelligent platforms for the identification of various pathogenic microorganisms towards rapid and accurate diagnosis of a wide range of infectious diseases.

Supporting Information.

The Supporting Information is available with open access at XXX

SEM images, TEM images, XPS spectrum, the k3-weighted k-space spectra of Fe_1-NC, the binding situation between Fe_1-NC and the microorganism, the colorimetric response pattern obtained by the functionalized Fe_1-NC with microorganism, discrimination performance of three unsupervised dimension-reducing algorithms, optimization of the experimental conditions for the sensing systems, validation of the colorimetric sensor in human urine.

Author Information

Corresponding Author

Chunxian Guo, School of Materials Science and Engineering, Suzhou University of Science and Technology, Suzhou, Jiangsu 215009, China E-mail: cxguo@usts.edu.cn

Hong Bin Yang, School of Materials Science and Engineering, Suzhou University of Science and Technology, Suzhou, Jiangsu 215009, China E-mail: yanghb@mail.usts.edu.cn

Fang Xin Hu, School of Materials Science and Engineering, Suzhou University of Science and Technology, Suzhou, Jiangsu 215009, China E-mail: hufx278@usts.edu.cn

Luigi G. Occhipinti, Department of Engineering, University of Cambridge, Cambridge CB3 0FA, United Kingdom. E-mail: lgo23@cam.ac.uk

Author Contributions

J.Y. and G. L. contributed equally to this work. J.Y., H. Y. and F. H. initiated the concept and designed the studies; J. Y. and G. L. led the experiments and collected the overall data; G. L. and G. H. contributed to the colorimetric sensor array design and developed; D. X. contributed to clinical sample analysis; J. Y. carried out the construction of mathematical detection model. X. S. performed the X-ray absorption experiments. Y. Z., S. C. and Y. L. contributed to materials characterization and experimental data analysis. J. Y., C. G., H. Y., and F. H. co-wrote the manuscript., C.

G., H. Y and F. H. supervised the work; L.G.O. analysed the data and revised the manuscript; All authors have read and agreed to the final version of this manuscript.

Notes

The authors declare no competing financial interest.

Acknowledgments

This work was supported by the National Natural Science Foundation of China (22075195 and 21705115), the National Key Research and Development Program of China (2021YFA0910403) and the Natural Science research Foundation of Jiangsu Higher Education Institutions (23KJB150034). The Qinglan Project of Jiangsu Province for F.X.H. The lifting project of youth science and technology talent of Suzhou Science and Technology Association for F.X.H. Jiangsu Laboratory for Biochemical Sensing and Biochip, Collaborative Innovation Center of Technology and Material of Water Treatment. Special thanks are due to the X-ray absorption spectroscopy data analysis from Photon Science Research center for Carbon Dioxide.

References

(1) May, M. Tomorrow's biggest microbial threats. *Nat. Med.* **2021**, *27* (3), 358-359. DOI: 10.1038/s41591-021-01264-2.

(2) Jones-Freeman, B.; Chonwerawong, M.; Marcelino, V. R.; Deshpande, A. V.; Forster, S. C.; Starkey, M. R. The microbiome and host mucosal interactions in urinary tract diseases. *Mucosal Immunol.* **2021**, *14* (4), 779-792. DOI: 10.1038/s41385-020-00372-5.

(3) Ambite, I.; Butler, D.; Wan, M. L. Y.; Rosenblad, T.; Tran, T. H.; Chao, S. M.; Svanborg, C. Molecular determinants of disease severity in urinary tract infection. *Nat. Rev. Urol.* **2021**, *18* (8), 468-486. DOI: 10.1038/s41585-021-00477-x.

(4) Russell, S. K.; Harrison, J. K.; Olson, B. S.; Lee, H. J.; O'Brien, V. P.; Xing, X.; Livny, J.; Yu, L.; Roberson, E. D. O.; Bomjan, R.; et al. Uropathogenic Escherichia coli infection-induced epithelial trained immunity impacts urinary tract disease outcome. *Nat. Microbiol.* **2023**, *8* (5), 875-888. DOI: 10.1038/s41564-023-01346-6.

(5) Mendive-Tapia, L.; Mendive-Tapia, D.; Zhao, C.; Gordon, D.; Benson, S.; Bromley, M. J.; Wang, W.; Wu, J.; Kopp, A.; Ackermann, L.; et al. Rational design of Phe-BODIPY amino acids as fluorogenic building blocks for peptide-based detection of urinary tract Candida infections. *Angew. Chem. Int. Ed.* **2022**, *61* (17), e202117218. DOI: 10.1002/anie.202117218.

(6) Flores-Mireles, A. L.; Walker, J. N.; Caparon, M.; Hultgren, S. J. Urinary tract infections: epidemiology, mechanisms of infection and treatment options. *Nat. Rev. Microbiol.* **2015**, *13* (5), 269-284. DOI: 10.1038/nrmicro3432.

(7) Fisher, M. C.; Alastruey-Izquierdo, A.; Berman, J.; Bicanic, T.; Bignell, E. M.; Bowyer, P.; Bromley, M.; Bruggemann, R.; Garber, G.; Cornely, O. A.; et al. Tackling the emerging threat of antifungal resistance to human health. *Nat. Rev. Microbiol.* **2022**, *20* (9), 557-571. DOI: 10.1038/s41579-022-00720-1.

(8) Ma, Y.; Guo, Z.; Xia, B.; Zhang, Y.; Liu, X.; Yu, Y.; Tang, N.; Tong, X.; Wang, M.; Ye, X.; et al. Identification of antimicrobial peptides from the human gut

microbiome using deep learning. *Nat. Biotechnol.* **2022**, *40* (6), 921-931. DOI: 10.1038/s41587-022-01226-0.

(9) Davenport, M.; Mach, K. E.; Shortliffe, L. M. D.; Banaei, N.; Wang, T. H.; Liao, J. C. New and developing diagnostic technologies for urinary tract infections. *Nat. Rev. Urol.* **2017**, *14* (5), 296-310. DOI: 10.1038/nrurol.2017.20.

(10) Markus, H.; Zhao, J.; Contente-Cuomo, T.; Stephens, M. D.; Raupach, E.; Odenheimer-Bergman, A.; Connor, S.; McDonald, B. R.; Moore, B.; Hutchins, E.; et al. Analysis of recurrently protected genomic regions in cell-free DNA found in urine. *Sci. Transl. Med.* **2021**, *13* (581), eaaz3088. DOI: doi:10.1126/scitranslmed.aaz3088.

(11) Aghazadeh, A.; Lin, A. Y.; Sheikh, M. A.; Chen, A. L.; Atkins, L. M.; Johnson, C. L.; Petrosino, J. F.; Drezek, R. A.; Baraniuk, R. G. Universal microbial diagnostics using random DNA probes. *Sci. Adv.* **2016**, *2* (9), e1600025. DOI: doi:10.1126/sciadv.1600025.

(12) Yang, Z.; Mao, S.; Wang, L.; Fu, S.; Dong, Y.; Jaffrezic-Renault, N.; Guo, Z., CRISPR/Cas and argonaute-based biosensors for pathogen detection. ACS Sensors 2023, 8 (10), 3623-3642. DOI: https://doi.org/10.1021/acssensors.3c01232

(13) Dou, W.-T.; Wang, X.; Liu, T.; Zhao, S.; Liu, J.-J.; Yan, Y.; Li, J.; Zhang, C.-Y.; Sedgwick, A. C.; Tian, H.; et al. A homogeneous high-throughput array for the detection and discrimination of influenza A viruses. *Chem* **2022**, *8* (6), 1750-1761. DOI: https://doi.org/10.1016/j.chempr.2022.03.012.

(14) Liu, H.; Li, Z.; Shen, R.; Li, Z.; Yang, Y.; Yuan, Q. Point-of-care pathogen testing using photonic crystals and machine vision for diagnosis of urinary tract infections. *Nano Lett.* **2021**, *21* (7), 2854-2860. DOI: 10.1021/acs.nanolett.0c04942.

(15) Hu, X.-L.; Gan, H.-Q.; Qin, Z.-Y.; Liu, Q.; Li, M.; Chen, D.; Sessler, J. L.; Tian, H.; He, X.-P. Phenotyping of Methicillin-resistant Staphylococcus aureus using a ratiometric sensor array. *J. Am. Chem. Soc.* **2023**, *145* (16), 8917-8926. DOI: 10.1021/jacs.2c12798.

(16) Yu, T.; Su, S.; Hu, J.; Zhang, J.; Xianyu, Y. A new strategy for microbial taxonomic identification through micro-biosynthetic gold nanoparticles and machine learning. *Adv. Mater.* **2022**, *34* (11), 2109365. DOI: https://doi.org/10.1002/adma.202109365.

(17) Yang, J.; Lu, S.; Chen, B.; Hu, F.; Li, C.; Guo, C. Machine learning-assisted optical nano-sensor arrays in microorganism analysis. *Trends Anal. Chem.* **2023**, *159*. DOI: 10.1016/j.trac.2023.116945.

(18) Han, J.; Cheng, H.; Wang, B.; Braun, M. S.; Fan, X.; Bender, M.; Huang, W.; Domhan, C.; Mier, W.; Lindner, T.; et al. A Polymer/peptide complex-based sensor array that discriminates bacteria in urine. *Angew. Chem. Int. Ed.* **2017**, *56* (48), 15246-15251. DOI: https://doi.org/10.1002/anie.201706101.

(19) Wang, J.; Jiang, Z.; Wei, Y.; Wang, W.; Wang, F.; Yang, Y.; Song, H.; Yuan, Q. Multiplexed identification of bacterial biofilm infections based on machine-learning-aided lanthanide encoding. *ACS Nano* **2022**, *16* (2), 3300-3310. DOI: 10.1021/acsnano.1c11333.

(20) Tomita, S.; Kusada, H.; Kojima, N.; Ishihara, S.; Miyazaki, K.; Tamaki, H.; Kurita, R. Polymer-based chemical-nose systems for optical-pattern recognition of gut microbiota. *Chem. Sci.* **2022**, *13* (20), 5830-5837, 10.1039/D2SC00510G. DOI: 10.1039/D2SC00510G.

(21) Zhou, C.; Xu, W.; Zhang, P.; Jiang, M.; Chen, Y.; Kwok, R. T. K.; Lee, M. M. S.; Shan, G.; Qi, R.; Zhou, X.; et al. Engineering sensor arrays using aggregation-induced emission luminogens for pathogen identification. *Adv. Funct. Mater.* **2019**, *29* (4). DOI: 10.1002/adfm.201805986.

(22) Kim, M. S.; Lee, J.; Kim, H. S.; Cho, A.; Shim, K. H.; Le, T. N.; An, S. S. A.; Han, J. W.; Kim, M. I.; Lee, J. Heme cofactor-resembling Fe-N single site embedded graphene as nanozymes to selectively detect H_2O_2 with High sensitivity. *Adv. Funct. Mater.* **2020**, *30* (1), 1905410. DOI: https://doi.org/10.1002/adfm.201905410.

(23) Hu, F. X.; Hu, G.; Wang, D. P.; Duan, X.; Feng, L.; Chen, B.; Liu, Y.; Ding, J.; Guo, C.; Yang, H. B. Integrated biochip-electronic system with single-atom nanozyme for in vivo analysis of nitric oxide. *ACS Nano* **2023**, *17* (9), 8575-8585. DOI: 10.1021/acsnano.3c00935.

(24) Li, Z.; Tian, E.; Wang, S.; Ye, M.; Li, S.; Wang, Z.; Ma, Z.; Jiang, G.; Tang, C.; Liu, K.; et al. Single-atom catalysts: promotors of highly sensitive and selective sensors. *Chem. Soc. Rev.* **2023**, *52* (15), 5088-5134, 10.1039/D2CS00191H. DOI: 10.1039/D2CS00191H.

(25) Teng, Z.; Zhang, Q.; Yang, H.; Kato, K.; Yang, W.; Lu, Y.-R.; Liu, S.; Wang, C.; Yamakata, A.; Su, C.; et al. Atomically dispersed antimony on carbon nitride for the

artificial photosynthesis of hydrogen peroxide. *Nat. Catal.* **2021**, *4* (5), 374-384. DOI: 10.1038/s41929-021-00605-1.

(26) Hu, F. X.; Hu, T.; Chen, S.; Wang, D.; Rao, Q.; Liu, Y.; Dai, F.; Guo, C.; Yang, H. B.; Li, C. M. Single-atom cobalt-based electrochemical biomimetic uric acid sensor with wide linear range and ultralow detection limit. *Nano-Micro Lett.* **2020**, *13* (1), 7. DOI: 10.1007/s40820-020-00536-9.

(27) Huang, L.; Chen, J.; Gan, L.; Wang, J.; Dong, S. Single-atom nanozymes. *Sci. Adv.* **2019**, *5* (5), eaav5490. DOI: doi:10.1126/sciadv.aav5490.

(28) Tian, R.; Ma, H.; Ye, W.; Li, Y.; Wang, S.; Zhang, Z.; Liu, S.; Zang, M.; Hou, J.; Xu, J.; et al. Se-containing MOF coated dual-Fe-atom nanozymes with multi-enzyme cascade activities protect against cerebral ischemic reperfusion injury. *Adv. Funct. Mater.* **2022**, *32* (36), 2204025. DOI: https://doi.org/10.1002/adfm.202204025.

(29) Yu, T.; Fu, Y.; He, J.; Zhang, J.; Xianyu, Y. Identification of antibiotic resistance in ESKAPE pathogens through plasmonic nanosensors and machine learning. *ACS Nano* **2023**, *17* (5), 4551-4563. DOI: 10.1021/acsnano.2c10584.

(30) Dawson, W. M.; Shelley, K. L.; Fletcher, J. M.; Scott, D. A.; Lombardi, L.; Rhys, G. G.; LaGambina, T. J.; Obst, U.; Burton, A. J.; Cross, J. A.; et al. Differential sensing with arrays of de novo designed peptide assemblies. *Nat. Commun.* **2023**, *14* (1), 383. DOI: 10.1038/s41467-023-36024-y.

(31) Yin, F.; Zhao, H.; Lu, S.; Shen, J.; Li, M.; Mao, X.; Li, F.; Shi, J.; Li, J.; Dong, B.; et al. DNA-framework-based multidimensional molecular classifiers for cancer

diagnosis. *Nat. Nanotechnol.* **2023**, *18* (6), 677-686. DOI: 10.1038/s41565-023-01348-9.

(32) Zhang, C.; Zhao, Y.; Xu, X.; Xu, R.; Li, H.; Teng, X.; Du, Y.; Miao, Y.; Lin, H.-c.; Han, D. Cancer diagnosis with DNA molecular computation. *Nat. Nanotechnol.* **2020**, *15* (8), 709-715. DOI: 10.1038/s41565-020-0699-0.

(33) Kiselev, V. Y.; Andrews, T. S.; Hemberg, M. Challenges in unsupervised clustering of single-cell RNA-seq data. *Nat. Rev. Genet.* **2019**, *20* (5), 273-282. DOI: 10.1038/s41576-018-0088-9.

(34) Sakaue, S.; Hirata, J.; Kanai, M.; Suzuki, K.; Akiyama, M.; Lai Too, C.; Arayssi, T.; Hammoudeh, M.; Al Emadi, S.; Masri, B. K.; et al. Dimensionality reduction reveals fine-scale structure in the Japanese population with consequences for polygenic risk prediction. *Nat. Commun.* **2020**, *11* (1), 1569. DOI: 10.1038/s41467-020-15194-z.

(35) Ma, Q.; Zhang, M.; Zhang, C.; Teng, X.; Yang, L.; Tian, Y.; Wang, J.; Han, D.; Tan, W. An automated DNA computing platform for rapid etiological diagnostics. *Sci. Adv.* **2022**, *8* (47), eade0453. DOI: doi:10.1126/sciadv.ade0453.

(36) Huang, B.; Chau, S. W. H.; Liu, Y.; Chan, J. W. Y.; Wang, J.; Ma, S. L.; Zhang, J.; Chan, P. K. S.; Yeoh, Y. K.; Chen, Z.; et al. Gut microbiome dysbiosis across early Parkinson's disease, REM sleep behavior disorder and their first-degree relatives. *Nat. Commun.* **2023**, *14* (1), 2501. DOI: 10.1038/s41467-023-38248-4.

(37) Chen, M.; Zhang, J.; Qi, J.; Dong, R.; Liu, H.; Wu, D.; Shao, H.; Jiang, X. Boronic acid-decorated multivariate photosensitive metal-organic frameworks for combating

multi-drug-resistant bacteria. *ACS Nano* **2022**, *16* (5), 7732-7744. DOI: 10.1021/acsnano.1c11613.

(38) Pidgeon, S. E.; Pires, M. M. Vancomycin-dependent response in live drug-resistant bacteria by metabolic labeling. *Angew. Chem. Int. Ed.* **2017**, *56* (30), 8839-8843. DOI: https://doi.org/10.1002/anie.201704851.

(39) Wang, W.; Lin, L.; Du, Y.; Song, Y.; Peng, X.; Chen, X.; Yang, C. J. Assessing the viability of transplanted gut microbiota by sequential tagging with D-amino acid-based metabolic probes. *Nat. Commun.* **2019**, *10* (1), 1317. DOI: 10.1038/s41467-019-09267-x.

(40) Tang, N.; Zhang, R.; Zheng, Y.; Wang, J.; Khatib, M.; Jiang, X.; Zhou, C.; Omar, R.; Saliba, W.; Wu, W.; et al. Highly efficient self-healing multifunctional dressing with antibacterial activity for sutureless wound closure and infected wound monitoring. *Adv. Mater.* **2022**, *34* (3), 2106842. DOI: https://doi.org/10.1002/adma.202106842.

(41) Yang, H. B.; Hung, S.-F.; Liu, S.; Yuan, K.; Miao, S.; Zhang, L.; Huang, X.; Wang, H.-Y.; Cai, W.; Chen, R.; et al. Atomically dispersed Ni(i) as the active site for electrochemical CO_2 reduction. *Nat. Energy* **2018**, *3* (2), 140-147. DOI: 10.1038/s41560-017-0078-8.

(42) Wan, X.; Liu, X.; Li, Y.; Yu, R.; Zheng, L.; Yan, W.; Wang, H.; Xu, M.; Shui, J. Fe-N-C electrocatalyst with dense active sites and efficient mass transport for high-performance proton exchange membrane fuel cells. *Nat. Catal.* **2019**, *2* (3), 259-268. DOI: 10.1038/s41929-019-0237-3.

(43) Xiong, Y.; Li, H.; Liu, C.; Zheng, L.; Liu, C.; Wang, J.-O.; Liu, S.; Han, Y.; Gu, L.; Qian, J.; et al. Single-atom Fe catalysts for Fenton-like reactions: roles of different N species. *Adv. Mater.* **2022**, *34* (17), 2110653. DOI: https://doi.org/10.1002/adma.202110653.

(44) Qin, J.; Han, B.; Liu, X.; Dai, W.; Wang, Y.; Luo, H.; Lu, X.; Nie, J.; Xian, C.; Zhang, Z. An enzyme-mimic single Fe-N_3 atom catalyst for the oxidative synthesis of nitriles via C-C bond cleavage strategy. *Sci. Adv.* **2022**, *8* (40), eadd1267. DOI: doi:10.1126/sciadv.add1267.

(45) Chen, Y. E.; Fischbach, M. A.; Belkaid, Y. Skin microbiota-host interactions. *Nature* **2018**, *553* (7689), 427-436. DOI: 10.1038/nature25177.

(46) Harris-Tryon, T. A.; Grice, E. A. Microbiota and maintenance of skin barrier function. *Science* **2022**, *376* (6596), 940-945. DOI: doi:10.1126/science.abo0693.

(47) Lopez, R.; Wang, R.; Seelig, G. A molecular multi-gene classifier for disease diagnostics. *Nat. Chem.* **2018**, *10* (7), 746-754. DOI: 10.1038/s41557-018-0056-1.